Chinese Chemical Letters 37 (2026) 110668

Contents lists available at ScienceDirect

Chinese Chemical Letters

journal homepage: www.elsevier.com/locate/cclet

Facet-dominant dual-selective sensing performance to HF and NO of Pt/TiO_2 film *via* phase transition

Xilong Lu[a,1], Liwen Mao[a,1], Yiming Liu[a], Zhenliang Dong[a], Tiange Gao[a], Libing Zheng[b,d], Peng Huang[c], Yueling Bai[a], Yiling Liu[c,*], Qingmin Hu[a,*], Jiaqiang Xu[a,*]

[a] *NEST Lab, Department of Physics, Department of Chemistry, Institute for Sustainable Energy, Collage of Sciences, Shanghai University, Shanghai 200444, China*
[b] *Institute of Electrical Engineering, Chinese Academy of Sciences (CAS), Beijing 100190, China*
[c] *National Institute of Metrology, Beijing 100029, China*
[d] *University of Chinese Academy of Science, Beijing 100083, China*

ARTICLE INFO

Article history:
Received 14 September 2024
Revised 7 November 2024
Accepted 21 November 2024
Available online 26 November 2024

Keywords:
Amorphous and crystal TiO_2
Atomic layer deposition
Phase transition
Strong metal support
Interaction (SMSI)
Precisely fabrication
HF and NO sensor

ABSTRACT

The surficial inherent properties of TiO_2 like exposed facet and crystalline state are vital for their surface reactions. However, efficiently controlling the specific crystal structure and the exposed crystal surface still faces big challenge. Here, the controlled solid phase transition of amorphous TiO_2 to crystalline phase with exposed crystal facet (001) is achieved by photo-assisted atomic layer deposition (ALD) Pt process. Significantly, the obtained Pt/TiO_2 film *via* photo-assisted treatment exhibits high sensing performance to NO and HF, and shows a lower optimized working temperature. The enhanced sensing performance is attributed to the metal-support strong interaction under oxidative atmosphere (O-SMSI). The facet effects leading to the unique distribution of charges at the interface combined with the catalytic effects result in the high sensing performance. This work provides a novel phase transition engineering strategy for regulating TiO_2 from amorphous to crystalline phase, and the controllable synthesis of high Pt monatomic loading on TiO_2 *via* ALD, which are critical for the accurate synthesis of efficient sensing and catalytic nanomaterials.

© 2025 Published by Elsevier B.V. on behalf of Chinese Chemical Society and Institute of Materia Medica, Chinese Academy of Medical Sciences.

Titanium dioxide (TiO_2) is widely used in catalysts support, gas sensors and photocatalysts due to its advantages such as low cost, photo-responsive, and high chemical and thermal stability [1–3]. It has been reported that the crystalline structure and the exposed facets of TiO_2 play important and even dominated roles in adsorption of reactant and the surficial reactions [4–6]. The Co single atoms on surface of brookite TiO_2 show high active oxygen evolution reaction [5]. Ru/rutile-TiO_2 shows high CO_2 conversion rate and selectivity to methane. However, Ru/anatase-TiO_2 shows low CO_2 conversion rate and selectivity to CO [4]. Pt located on different facet of TiO_2 show different CO catalytic performance [7]. TiO_2 is also one typical reductive support and leads to the strong metal–support interaction (SMSI) between the metal sites and TiO_2, regulating the catalytic performance.

Amorphous TiO_2 has also displayed advantages in application due to its special physicochemical properties such as high adsorption capacity [8,9]. However, amorphous TiO_2 is thermodynamic instable and that could transform to crystalline TiO_2 with exposed thermodynamically stable (101) facets [10,11]. In other words, the reported reactive (001) facet of crystalline TiO_2 usually diminishes rapidly due to the minimization of surface energy [12–14]. Phase transition from amorphous to crystalline has been proved as a promising method to fabricate active materials and modulate the response of materials by changing the physical properties like optical dielectric constant [15]. Though the phase transition of crystalline TiO_2 has been reported, however, the selective regulation from amorphous to crystalline TiO_2 remains ambiguous.

Herein, we employed a photo-assistant atomic layer deposition process to fabricate the TiO_2 sensing film *via* transformation of amorphous to specific crystalline TiO_2 directly on the micro-electromechanical systems (MEMS) as shown in Fig. S1 (Supporting information). With help of photo assistant, the specific crystalline TiO_2 film was fabricated during ALD Pt single atoms/clusters. Compared with bared amorphous TiO_2 film and conventional ALD Pt/TiO_2, the working temperature decreased from 370 °C (bared amorphous TiO_2) and 320 °C (Pt/TiO_2) to 260 °C for photo-assisted Pt/TiO_2. Photo-assisted Pt/TiO_2 maximized the utilization and re-

* Corresponding authors.
E-mail addresses: liuyl@nim.ac.cn (Y. Liu), huqingmin@shu.edu.cn (Q. Hu), xujiaqiang@shu.edu.cn (J. Xu).
[1] These authors contributed equally to this work.

https://doi.org/10.1016/j.cclet.2024.110668
1001-8417/© 2025 Published by Elsevier B.V. on behalf of Chinese Chemical Society and Institute of Materia Medica, Chinese Academy of Medical Sciences.

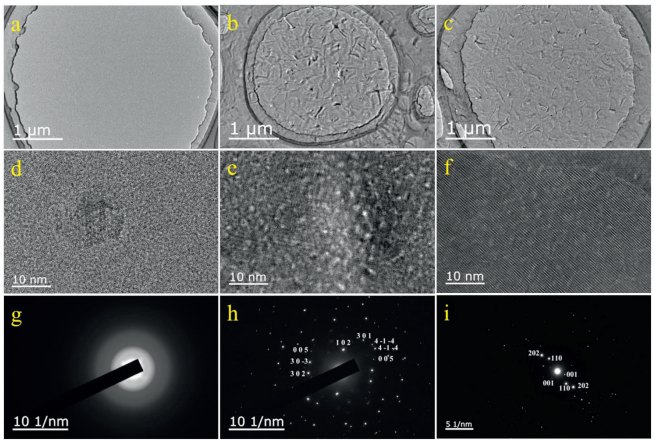


Fig. 1. The TEM, HRTEM and SAED images for (a, d, g) Ti400, (b, e, h) Ti400Pt40 and (c, f, i) p-Ti400Pt8, respectively.

duced loading of Pt with a factor of 5 times. With series characterizations, the photo-assisted ALD result in the selective transformation of TiO_2 from amorphous to crystalline with high active (001) facets. The unique electronic structure between highly dispersed Pt and TiO_2 is the main reasons for the preferred adsorption of HF and NO. The photo-assisted ALD offers a novel method to increase the dispersion of metal catalyst and regulate the transformation of amorphous metal oxide film, exhibiting broad potential application in design catalysts and sensing materials.

Transmission electron microscopy (TEM) is employed to characterize the morphology evolution of the samples. As shown in Fig. 1, the bare TiO_2 film was initially amorphous. With deposition of ALD Pt, the films transfer to a crystalline TiO_2. It is found that amorphous TiO_2 films become to more structured crystalline films with photo-assisted ALD Pt compared with Pt/TiO_2 film without photo-assistant. The Pt nanoparticles were observed in the HAADF-STEM images (Fig. S2 in Supporting information). This should be attributed to the photo assistant ALD Pt enhanced the SMSI effects which leads to transformation of TiO_2 from amorphous to crystalline with (001) facet exposed. Selected area electron diffraction (SAED) was used to further confirm the transformation of TiO_2. It is found that amorphous TiO_2 transfers to Ti_5O_9 with P1 space group during the deposition of ALD Pt from the Fig. 1 and Table S1 (Supporting information). With the introduction of photo-assisted process, the TiO_2 with (001) facet exposed C2/m space group because the Pt located on the amorphous TiO_2 decreased the energy barrier for oxidative strong metal support interaction (O-SMSI) with O_3 atmosphere [7,14]. And the phase transition with photo-assisted process is the main reason for the formation of photo active (001) facet. It should be caused by the strong metal support interaction, leading to the reconstruction of TiO_2 [16].

CO diffuse reflectance infrared Fourier transform spectroscopy (CO-DRIFTS) measurements were performed to further identify the atomic geometry configuration of Pt on TiO_2 film in Ti400Pt40 and p-Ti400Pt8. As shown in Fig. S3 (Supporting information), CO adsorption peaks on Ti400Pt40 and p-Ti400Pt8 locate at 2080–2090 cm^{-1} and 2100 cm^{-1}, respectively. The strong and broad vibration of Ti400Pt40 is attributed to linearly CO adsorption on Pt single atoms and Pt clusters. CO peak at 2100 cm^{-1} for p-Ti400Pt8 is ascribed to CO linearly adsorption on Pt single atoms or small clusters [17]. The CO-DRIFTS indicate p-Ti400Pt8 consists of Pt single atoms or small cluster [18,19], which is consistent with TEM results, revealing the highly dispersed distribution of Pt.

The spatial distribution of temperature after loading the sensing materials is vital for the sensing performance because the nonequilibrium of temperature leads the difference in response. Spatial distribution of temperature for Pt25 film obtained by dip-coating and ALD TiO_2 were employed to confirm the different between ALD and traditional films. As shown in Figs. S4a and b (Supporting information), the spatial distribution of sensing materials and temperature is non-uniform. For ALD TiO_2 film, it is transparent as shown in Fig. S4c (Supporting information). And transient spatial distribution of temperature results confirmed that it is uniform for ALD film and the temperature reach 300 °C with 50 ms (Fig. S4d in Supporting information). The uniform spatial distribution of temperature of ALD TiO_2 based film would lead to the high utilization of sensing materials on MEMS. However, pristine amorphous TiO_2 films are not stable (Fig. S5 in Supporting information).

The optimizing of the TiO_2 thickness was done by change ALD TiO_2 cycle numbers (Fig. S6 in Supporting information). 400 ALD TiO_2 film was selected for further studies in order to obtain the high sensing performance to HF and NO. Amorphous TiO_2 shows high sensing performance for NO. However, amorphous TiO_2 was not stable and transform to anatase TiO_2 film at optimized working temperature (370 °C).

ALD Pt was decorated on the TiO_2 sensing film to enhance the sensing performance due to its catalytic activity and spillover effect [20,21]. As shown in Fig. S7a (Supporting information), the sensing performance to NO of TiO_2 with different cycle Pt at various working temperature was displayed. Ti400Ptx show the higher sensing performance to NO and has a lower optimal temperature (320 °C) compared with amorphous TiO_2 film (370 °C). The Ti400Ptx film selective response values to NO and HF are shown in Fig. S7b (Supporting information). And the sensing performance to NO and HF with the Pt ALD cycle number were displayed in Figs. S7c and d (Supporting information). It is found that Ti400Pt40 shows the best sensing performance to NO (0.57@10 ppm). However, the sensing performance to HF decreased with increase of Pt ALD cycle number, showing higher sensing performance with 5 cycles ALD Pt (1.12@7 ppm).

The response time and recovery time to NO of Ti400Pt40 sample are 3 s and 3 s (Fig. S7e in Supporting information), respectively. The response-recovery performance to HF of Ti400Pt5 shows the similarly sensing performance to that of amorphous TiO_2 film (Fig. S7f in Supporting information). The dynamic transients to NO (for Ti400Pt40 and Ti400) in range of 10–300 ppm (Fig. S7g in Supporting information) and that to HF (for Ti400Pt5 and Ti400) in range of 1–7 ppm (Fig. S7h in Supporting information) were further evaluated. The sensor responses increase with increase of gas concentration. The relationship between concentration and response for NO and HF were calculated with linearly fitting (Fig. S8 in Supporting information). The R^2 are 0.991 and 0.996 for HF (1–7 ppm) and NO (10–80 ppm), respectively. HF displays the strong positive linear relationship between concentration and response, however, the NO shows strong negative linear relationship between concentration and response. Resistance reproducibility of Ti400Pt40 and Ti400 confirmed sensing stability and the lower resistance for Ti400Pt5 compared with Ti400. The above sensing performance reveals that the decoration of Pt play the role in absorbed sites for NO and HF, and could enhancing gas sensitivity.

To further improve the sensing performance of the obtained sensors, preparation of high dispersive Pt single atoms or cluster with high loading is an effective method. And exposure of active facet could also enhance the gas sensitivity or selectivity. Photo-assisted ALD Pt was employed to increase the dispersive Pt singe atoms/clusters as well as selective phase transition of amorphous TiO_2. The sensing performance to NO and HF for p-Ti400Pty ($y = 5$, 8, 12, 16 and 20) at different working temperature was displayed in Figs. 2a and b. For different p-Ti400Pty sensors, the sensing value to NO was relatively stable within the tested temperature, and p-Ti400Pt8 shows the biggest sensing value ($R_a/R_g = 0.5$). The response value for HF decreased as the temperature is higher

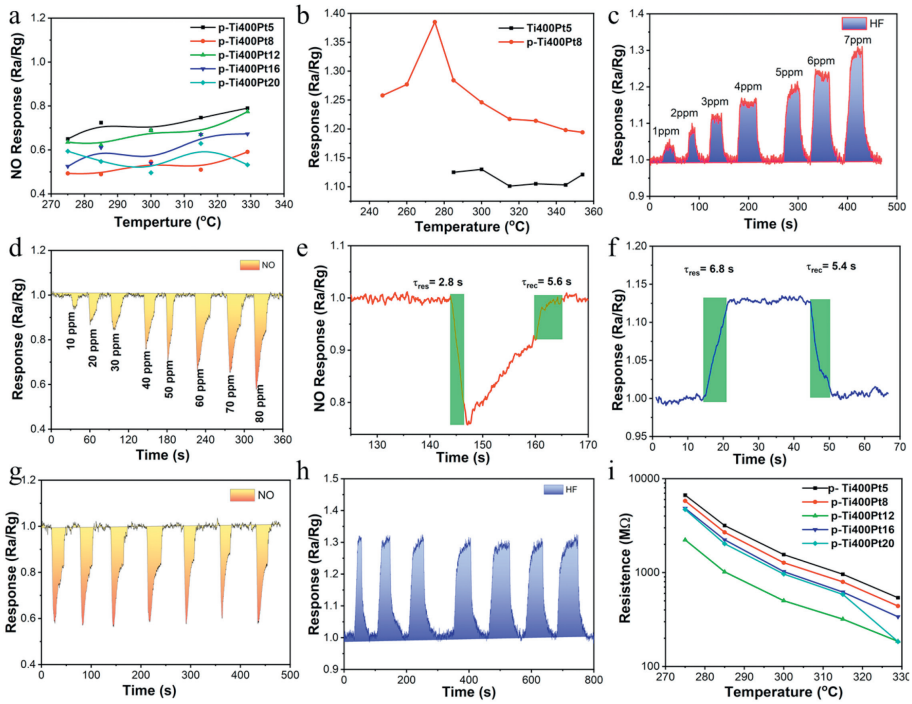


Fig. 2. Sensing performance of p-Ti400Ptx samples (x = 5, 8, 12, 16 and 20) of (a) 80 ppm NO and (b) 10 ppm HF at different working temperature. Dynamic sensing performance of (c) NO and (d) HF for p-Ti400Pt8. Response/recover performance for (e) NO and (f) HF. Dynamic sensing performance for (g) NO and (h) HF. (i) Resistance for p-Ti400Pty (y = 5, 8, 12, 16 and 20) at different working temperature.

than the optimized working temperature (280 °C). p-Ti400Pt8 shows the highest response to NO and HF as shown in Fig. S9 (Supporting information). It was attributed to the high content of Pt single atoms which plays as active sites to adsorb NO and HF. The dynamic transients to NO for p-Ti400Pt8 in range of 10–80 ppm (Fig. 2c) and that to HF in range of 1–7 ppm (Fig. 2d) were further evaluated. The sensor responses increase with increase of gas concentration. The relationship between concentration and response for NO and HF were calculated with linearly fitting (Fig. S10 in Supporting information). The R^2 are 0.996 and 0.986 for HF (1–7 ppm) and NO (10–80 ppm), respectively. HF displays the strong positive linear relationship between concentration and response, however, the NO shows strong negative linear relationship between concentration and response. The dynamic response–recovery curves to 50 ppm NO and 7 ppm HF were also shown in Figs. 2e and f. The response time of p-Ti400Pt8 sample is 2.8 s which is 1/3 of response time of bare TiO_2 film and the recovery time 5.6 s, respectively. The response-recovery time to HF of p-Ti400Pt8 is the 6.8 s and 5.4 s, respectively. Reproducibility of p-Ti400Pt8 for 80 ppm NO confirmed sensing stability (Fig. 2g), and it is higher (R_a/R_g is about 0.6 for 80 ppm) than that of Ti400Pt40 (R_a/R_g is about 0.6 for 200 ppm). That was similar to HF (Fig. 2h). The resistance for p-Ti400Ptx samples decreased as working temperature increasing (Fig. 2i). The enhanced sensing performance should be ascribed to the active facet (001) of TiO_2 and highly dispersed Pt which are beneficial for the adsorption of gases.

The X-ray photoelectron spectroscopy (XPS) was carried out to understand the sensing mechanism that the photo-assisted ALD Pt/TiO_2 result in high sensing performance with low content of Pt. It was obviously that O 1s peak is slightly higher for p-Ti400Pt8 and Ti400Pt40 compared with the initial amorphous TiO_2. Three peaks located at 530.05, 530.9 and 532.0 eV are corresponded to crystal lattice (O_L), oxygen vacancies (V_o) and chemisorbed oxygen (O_c), respectively [21–24]. It can be seen from Figs. 3a-c, the absorbed oxygen species and oxygen vacancies of Pt-Ti_5O_9 increased compared with pristine amorphous TiO_2 as shown in the inset of Fig. 3. With the photo-assisted ALD Pt, the absorbed oxygen species and oxygen vacancies of p-Ti400Pt8 sample decreased. The lower binding energy of p-Ti400Pt8 (Fig. 3d) will result in more electrons transferring to surface. The XPS results reveal that the oxygen vacancies and the absorbed surficial oxygen species may not the main reason for the enhanced sensing performance.

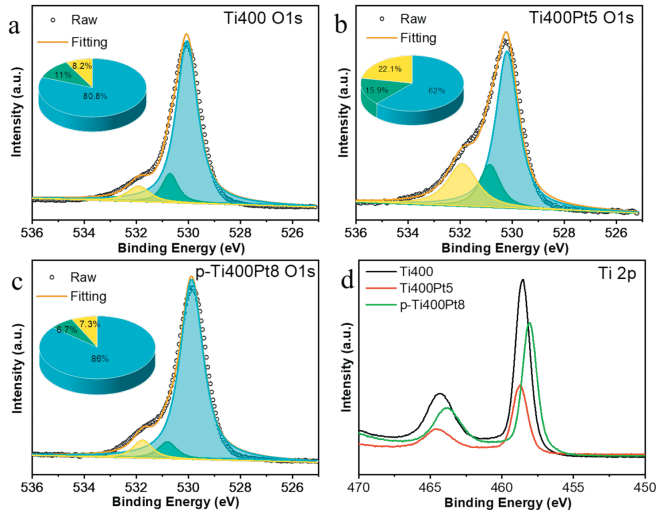


Fig. 3. The O 1s XPS spectra for amorphous (a) Ti400, (b) Ti400Pt5 and (c) p-Ti400Pt8, respectively. (d) The Ti 2p for different samples.

To further understand the sensing mechanism, density functional theory calculations were performed to investigate the influence of electronic structure and atomic configuration for gas adsorption and charge transfer. Electronic structures after decoration ALD Pt were firstly studied. From Fig. 4, the Bader charge analysis demonstrates that the addition of Pt leads to negative charge around Pt sites, which are beneficial for the formation of surficial

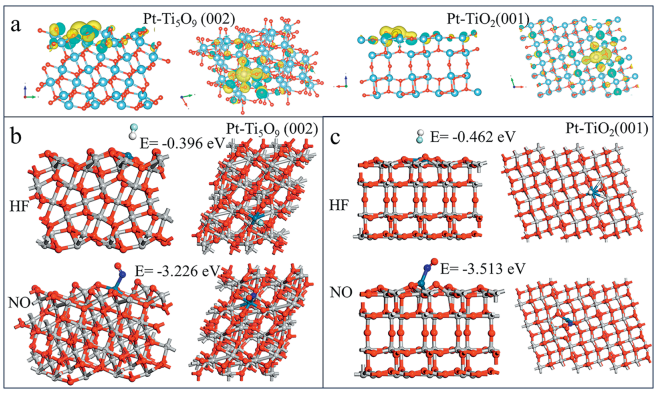


Fig. 4. (a) The Electronic structure for the samples with and without photo-assistant after ALD Pt, respectively (gray, red, and blue balls denote Ti, O, and Pt atoms, respectively. The yellow color means obtaining electrons and the light blue means losing electrons). (b, c) The absorbed atomic structure for HF and NO on Pt-Ti_5O_9 (002) and p-Ti400Pt8 with TiO_2(001) surface.

oxygen by electron transfer to oxygen [22,25]. The adsorption of HF and NO on Ti400Pt5 and p-Ti400Pt8 were also calculated by DFT calculation. The final atomic configuration was shown in Fig. 4, the negative electronic structures for Pt-TiO_2 based samples are in favor of adsorption for target gases. The p-Ti400Pt8 with (001) facet is preferred to absorb the HF (−0.462 eV) and NO (−3.513 eV) compared with Pt-Ti_5O_9 (002) with −0.396 eV for HF and −3.226 eV for NO, respectively. Facet dominated metal supported strong interaction (SMSI) results in redistribution of electrons between Pt and TiO_2 [17,26], further leading to stronger adsorption for HF and NO, which is the main reason for the higher sensing performance.

From the above results, the existence of Pt can enhance the gas sensitivity, plays the role in presenting absorbed sites for NO and HF. Combination of the active facet (001) of TiO_2 and highly dispersed Pt is beneficial for the adsorption of NO and HF. However, the oxygen vacancies and the absorbed surficial oxygen species of p-Ti400Pt8 are smaller than those of Ti400Pt5. This result demonstrates that oxygen vacancies and the absorbed surficial oxygen species may not the main reason for the enhanced sensing performance. From the above results, the NO and HF competes with adsorbed oxygen species [27–29]. The proposed sensing mechanism for NO and HF are shown in Eqs. S1-S5 (Supporting information).

In summary, the precise regulation of TiO_2 thin films from amorphous structure to specific crystal structure was realized through O-SMSI action, and the loading of dispersive Pt sites was effectively improved *via* the photo-assisted ALD. Its optimal working temperature reduces from the original 370 °C to 260 °C, and the gas sensitive properties are improved. The interfacial charge distribution and the adsorption of target molecules are improved effectively by regulating the interaction of metal carriers. This work provides useful guidance for the preparation of crystal firms, interfacial sites and single atoms.

Declaration of competing interest

The authors declare that they have no known competing financial interests or personal relationships that could have appeared to influence the work reported in this paper.

CRediT authorship contribution statement

Xilong Lu: Writing – original draft, Methodology, Data curation. **Liwen Mao:** Writing – original draft, Formal analysis, Data curation. **Yiming Liu:** Writing – original draft, Visualization, Validation, Formal analysis, Data curation. **Zhenliang Dong:** Visualization, Formal analysis, Data curation. **Tiange Gao:** Software, Methodology. **Libing Zheng:** Visualization, Validation, Methodology. **Peng Huang:** Validation, Methodology, Data curation. **Yueling Bai:** Validation. **Yiling Liu:** Writing – review & editing, Supervision. **Qingmin Hu:** Writing – review & editing, Validation, Supervision, Funding acquisition, Conceptualization. **Jiaqiang Xu:** Writing – review & editing, Supervision, Funding acquisition, Conceptualization.

Acknowledgments

The authors gratefully acknowledge financial support from National Key R&D Program of China (No. 2022YFC3320700), National Natural Science Foundation of China (Nos. 62271299 and 22302118) and China Postdoctoral Science Foundation (No. 2022M712019).

Supplementary materials

Supplementary material associated with this article can be found, in the online version, at doi:10.1016/j.cclet.2024.110668.

References

[1] J. Chen, Y. Kang, W. Zhang, et al., Angew. Chem. Int. Ed. 61 (2022) e202203022.
[2] L.N. Appelhans, P.S. Finnegan, L.T. Massey, et al., Sens. Actuator. B 228 (2016) 117–123.
[3] X. Zhang, Z. Yuan, J. Chen, et al., Catal. Today 340 (2020) 204–208.
[4] J. Zhou, Z. Gao, G. Xiang, et al., Nat. Commun. 13 (2022) 327.
[5] C. Liu, J. Qian, Y. Ye, et al., Nat. Catal. 4 (2020) 36–45.
[6] X. Zhang, Z. Li, W. Pei, et al., ACS Catal. 12 (2022) 3634–3643.
[7] Y. Zhang, A. Jia, Z. Li, Z. Yuan, W. Huang, ACS Catal. 13 (2022) 392–399.
[8] X. Wang, W. Shi, S. Wang, et al., J. Am. Chem. Soc. 141 (2019) 5856–5862.
[9] Z. Wang, C. Yang, T. Lin, et al., Energy Environ. Sci. 6 (2013) 3007.
[10] W. Lin, H. Zheng, P. Zhang, T. Xu, Appl. Catal. A: Gen. 521 (2016) 75–82.
[11] F. Pan, K. Wu, H. Li, G. Xu, W. Chen, Chemistry 20 (2014) 15095–15101.
[12] X.H. Yang, Z. Li, C. Sun, H.G. Yang, C. Li, Chem. Mater. 23 (2011) 3486–3494.
[13] B. Shao, W. Zhao, S. Miao, et al., Chin. J. Catal. 40 (2019) 1534–1539.
[14] H.G. Yang, C.H. Sun, S.Z. Qiao, et al., Nature 453 (2008) 638–641.
[15] C. Zheng, R.E. Simpson, K. Tang, et al., Chem. Rev. 122 (2022) 15450–15500.
[16] A. Beck, H. Frey, X. Huang, et al., Angew. Chem. Int. Ed. 62 (2023) e202301468.
[17] Q. Hu, S. Wang, Z. Gao, et al., Appl. Catal. B: Environ. 218 (2017) 591–599.
[18] J.C. Matsubu, V.N. Yang, P. Christopher, J. Am. Chem. Soc. 137 (2015) 3076–3084.
[19] X. Lan, K. Xue, T. Wang, J. Catal. 372 (2019) 49–60.
[20] Y. Xu, W. Zheng, X. Liu, et al., Mater. Horiz. 7 (2020) 1519–1527.
[21] S. Zhang, X. Chang, L. Zhou, X. Liu, J. Zhang, ACS Sens. 9 (2024) 2101–2109.
[22] Q. Hu, X. Lu, T. Gao, et al., Sens. Actuator. B 414 (2024) 135852.
[23] M. Guo, N. Luo, Y. Bai, et al., Sens. Actuator. B 398 (2024) 134151.
[24] Q. Hu, C. Wu, Z. Dong, et al., J Mater. Chem. A 10 (2022) 2786–2794.
[25] H. Cai, N. Luo, Q. Hu, et al., ACS Sens. 7 (2022) 1484–1494.
[26] S. Bernal, J.J. Calvino, M.A. Cauqui, et al., Catal. Today 77 (2003) 385–406.
[27] T.Y. Chang, A.K. Singh, J.H. Shao, et al., Appl. Surf. Sci. 637 (2023) 157929.
[28] G.C. Lu, X.H. Liu, W. Zheng, et al., Rare Metals 41 (2022) 1520–1528.
[29] Y. Zhang, B. Wang, S. Lv, et al., Sens. Actuator. B 361 (2022) 131736.